

# Effect of KCl deposits in high-temperature corrosion on chromium-rich steels in SO<sub>2</sub>-containing atmosphere

Phillip Kingsbery<sup>1,2</sup>  | Christiane Stephan-Scherb<sup>1,2</sup> 

<sup>1</sup>Department of Earth Science, Freie Universität Berlin, Berlin, Germany

<sup>2</sup>Division of Materialography, Fractography and Ageing of Engineered Materials, Bundesanstalt für Materialforschung und -prüfung, Berlin, Germany

## Correspondence

Phillip Kingsbery, Department of Earth Science, Freie Universität Berlin, Malteserstraße 74-100, 12247 Berlin, Germany.

Email: [phillip.kingsbery@fu-berlin.de](mailto:phillip.kingsbery@fu-berlin.de)

## Funding information

Deutsche Forschungsgemeinschaft, Grant/Award Number: DFG-416318834

## Abstract

High-temperature corrosion was studied under multiple chemical loads on ferritic-austenitic model alloys (Fe-13Cr, Fe-18Cr-12Ni, and Fe-25Cr-20Ni) with KCl deposit under 0.5% SO<sub>2</sub>/99.5% Ar gas atmosphere at 560°C. Post-exposure characterization was done by X-ray diffraction and scanning electron microscopy. In a pure SO<sub>2</sub>/Ar environment a protective Cr<sub>2</sub>O<sub>3</sub> scale was formed by all samples. The introduction of KCl deposits causes the scale to be nonprotective and multilayered, consisting of CrS, FeS, Cr<sub>2</sub>O<sub>3</sub>, Fe<sub>3</sub>O<sub>4</sub>, and Fe<sub>2</sub>O<sub>3</sub>. The impact of the microstructure and alloying elements is discussed.

## KEYWORDS

high-temperature corrosion, KCl, microstructure, SO<sub>2</sub>, steel alloy

## 1 | INTRODUCTION

The environmental impact of power generation has become one of the most important topics of the 21st century. One initiative to reduce the use of fossil fuels has been co-firing of coal power plants using biofuel, which consists of organic matter such as straw and wood. The use of biofuel presents new challenges to the materials used as boiler tubes due to the different chemical environments. The chemistry of biomass, wood, and straw, for example, is quite different from fossil fuels. In Germany, the main quantity of biomass types used for energy fabrication is ligneous fuels. Besides the main constituents carbon, oxygen, and hydrogen, a significant amount of KCl (e.g., straw: up to 1 wt%) can be present, which is known to cause severe deposit-induced corrosion.<sup>[1,2]</sup>

The corrosion resistance of high-temperature alloys used in energy applications depends on the Cr-content. Cr affects the corrosion resistance of steels in sulfidising

and oxidizing atmospheres. Hernas et al.<sup>[3]</sup> found that for steels with Cr contents between 8.96 wt% and 18.5 wt% the corrosion resistance increases with increasing Cr content in an N<sub>2</sub> + 9% O<sub>2</sub> + 0.2% HCl + 0.08% SO<sub>2</sub> atmosphere at 600°C and 700°C.

The effect of KCl deposits on the corrosion mechanism in a humid atmosphere has been studied by Lehmusto et al.<sup>[4]</sup> on Sanicro 28 at 550°C (20% O<sub>2</sub>; 10% H<sub>2</sub>O volumetric mixture), Pettersson<sup>[5]</sup> on Fe-18Cr-10Ni at 600°C (5% O<sub>2</sub>; 40% H<sub>2</sub>O volumetric mixture) and Jonsson et al.<sup>[6]</sup> on 304L at 600°C (5% O<sub>2</sub>; 40% H<sub>2</sub>O volumetric mixture). In the presence of oxygen and water, the KCl attacks Cr<sub>2</sub>O<sub>3</sub> to form K<sub>2</sub>CrO<sub>4</sub>, destroying the protective chromia scale. Karlsson et al.<sup>[7]</sup> studied the influence of SO<sub>2</sub> and KCl on the initial stages of corrosion of stainless steel 304L at 600°C in a volumetric mixture of 0.5% O<sub>2</sub> and 40% H<sub>2</sub>O.<sup>[7]</sup> The study by Karlsson et al.<sup>[7]</sup> showed, that the addition of SO<sub>2</sub> in a wet atmosphere leads to a decreased corrosion rate, in comparison to a

This is an open access article under the terms of the Creative Commons Attribution License, which permits use, distribution and reproduction in any medium, provided the original work is properly cited.

© 2022 The Authors. *Materials and Corrosion* published by Wiley-VCH GmbH.

KCl + H<sub>2</sub>O atmosphere. The lower corrosion rate was linked to the formation of K<sub>2</sub>SO<sub>4</sub>, which does not attack the protective Cr<sub>2</sub>O<sub>3</sub> scale to form K<sub>2</sub>CrO<sub>4</sub>, as is the case for an SO<sub>2</sub>-free atmosphere.

The studies on KCl induced corrosion, coupled with the humid atmosphere and under the influence of SO<sub>2</sub> did not include the consideration of different alloy microstructures (for instance ferritic–ferritic/austenitic). However, the impact of KCl in a dry, SO<sub>2</sub> containing atmosphere has not been studied. As SO<sub>2</sub> is a product of biomass combustion it is crucial to understand the corrosion mechanism of boiler tubes in SO<sub>2</sub> bearing atmospheres with and without KCl deposits. To gain insight into the corrosion mechanism this study will focus on model alloys derived off of commercially used steels for boiler tubes: X20, TP 347H, and HR3C.<sup>[8]</sup>

The goal of this study is to gain an understanding of the underlying mechanism of high-temperature corrosion, especially in the presence of salt deposits, considering active chloride corrosion, oxidation, and sulfidation. Furthermore, the impact of Cr and Ni in such environments on corrosion behavior is investigated.

## 2 | MATERIALS AND METHODS

### 2.1 | Materials

This study focuses on three model alloys purchased from HMW Hauner GmbH. All samples were vacuum-melted, mixed, hot, and cold rolled with minimum Fe purity of 99.95% and Cr, Ni purities of 99.9%. The chemical composition and phase of the microstructure are given in Table 1.  $\alpha$  denotes the body-centered cubic phase of iron (ferrite),  $\gamma$  the face-centered cubic phase (austenite). The microstructure was determined through light microscopy of the etched samples.

The utilized custom alloys are similar in composition to commercially used ones, namely, Fe–13Cr to X20 and Fe–25Cr–20Ni to HR3C.<sup>[8]</sup> The custom alloy Fe–18Cr–12Ni

**TABLE 1** Elemental composition of studied samples obtained by electron microprobe analysis on a JEOL JXA 8200 Superprobe utilizing ZAF correction, values given in wt%

Sample	Fe	Cr	Ni	Phase
Fe–13Cr	Bal.	13.5 ± 0.4	0.0 ± 0.0	$\alpha$
Fe–18Cr–12Ni	Bal.	18.5 ± 0.5	11.8 ± 0.2	$\alpha + \gamma$
Fe–25Cr–20Ni	Bal.	24.5 ± 0.7	19.1 ± 0.4	$\alpha + \gamma$

Note: ZAF is the abbreviation for the three effects impacting the characteristic X-ray intensity when performing quantitative analysis: atomic number(Z), absorption(A) and fluorescence(F).

is chosen as an intermediary alloy between Fe–13Cr and Fe–25Cr–20Ni, to show the effect of increasing Cr and Ni content and is comparable to alloy TP 347H.

### 2.2 | Sample pretreatment and exposure

The samples were cut into 10 × 20 × 3 mm coupons and ground to Grit 600/P1200.

The samples were exposed at 560°C for 330 h to a volumetric gas mixture of 0.5% SO<sub>2</sub>/99.5% Ar ( $p_{S_2} = 3.9 \times 10^{-11}$ ,  $p_{O_2} = 1.1 \times 10^{-16}$ , calculated using FactSage 8.0) in a tubular furnace. Exposure experiments with and without KCl deposits were performed. The atmosphere and flow rate are given in Table 2.

A schematic overview of the experimental setup is shown in Figure 1. The gas intake is regulated by a flow controller to ensure a well-defined gas mixture inside the furnace with a constant flow rate.

For the experiments including the KCl deposit, the samples were placed in alumina crucibles and partially embedded in KCl before being placed into the furnace (see Figure 1b). The crucibles and KCl were both dried in an oven for 1 day at 250°C before each experiment to purify the KCl from any adsorbed water according to DIN ISO 17224.<sup>[9]</sup>

### 2.3 | Sample post-characterization

After gas exposure, the surface of samples with KCl deposit was characterized by X-ray diffraction (XRD) using a Panalytical Empyrean diffractometer utilizing Cu K- $\alpha$  X-rays. The as-reacted KCl deposit was scraped off the alloys, together with the scale, and turned into a powder. This mixture was then analyzed in theta–2theta geometry.

Additionally, the surface was analyzed using scanning electron microscopy (SEM). Images of samples exposed to 0.5% SO<sub>2</sub>/99.5% Ar were obtained using a Tescan Vega 3 (Fe–13Cr) and Zeiss Sigma 300 VP (Fe–18Cr–12Ni, Fe–25Cr–20Ni). Samples exposed to KCl deposits were analyzed using a Zeiss Sigma 300 VP. The acceleration voltage was 20 kV for all samples.

Metallographic cross-sections were prepared by embedding the samples into an epoxy resin, ground, and

**TABLE 2** Corrosive atmosphere used in this study, values given in vol%

	Ar	SO <sub>2</sub>	Flow rate (m/s)
Corrosive atmosphere	99.5	0.5	1.4–1.5 × 10 <sup>-2</sup>

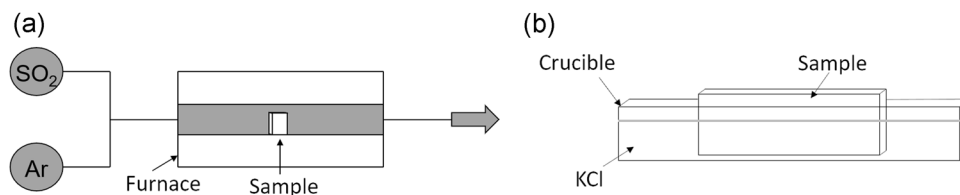


**FIGURE 1** Schematic drawing of experimental setups. (a) shows the oxidation simulation facility and (b) the way the sample is mounted within the crucible

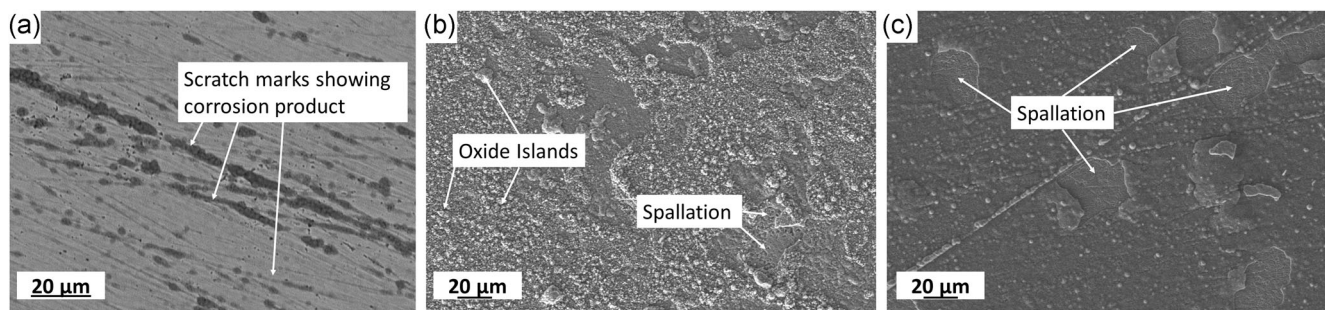


**FIGURE 2** Scanning electron microscopy-backscattered electron images showing the surface of samples exposed to 0.5% SO<sub>2</sub>/99.5% Ar for 330 h at 560°C. (a) Fe-13Cr, (b) Fe-18Cr-12Ni, and (c) Fe-25Cr-20Ni

finished with a 1 μm diamond suspension. For the KCl exposed samples, the entire preparation was done water-free, to preserve possible soluble phases. These samples were finished using P4000 SiC paper instead of the diamond suspension.

The cross-sections were carbon-coated to improve conductivity before analysis by SEM and energy dispersive X-ray analysis (EDX) using a Zeiss Sigma 300 VP and the equipped Quantax Xflash 60mm<sup>2</sup> detectors. Line scans were produced utilizing the EDX map data using Bruker's Esprit program.

## 3 | RESULTS

### 3.1 | 0.5% SO<sub>2</sub>/99.5% Ar

#### 3.1.1 | Surface structure and morphology postexposure

Initially, the effect of chromium content on oxidation/sulfidation (without KCl deposit) was investigated. The SEM backscattered electron (BSE) surface images of samples after exposure to 0.5% SO<sub>2</sub>/99.5% Ar are shown in Figure 2.

Fe-13Cr shows only slight surface damage by corrosion. The corrosion islands are localized close to scratches, which are artifacts of sample pretreatment.

Fe-18Cr-12Ni developed a large area showing oxide islands on the surface. Scratch marks cannot be seen

through the scale indicating a thicker scale compared to Fe-13Cr. Individual spots show spallation of the oxide scale.

Fe-25Cr-20Ni shows a continuous and smooth surface scale. However, the sample shows multiple areas with spallation.

#### 3.1.2 | Cross-section analysis

The SEM-BSE cross-section images of samples exposed to SO<sub>2</sub> are displayed in Figure 3.

Fe-13Cr (Figure 3a) shows a very thin (<1 μm) oxide layer and comparatively larger islands (~2 μm).

Fe-18Cr-12Ni (Figure 3b) and Fe-25Cr-20Ni (Figure 3c) show a thin, continuous layer (<1 μm) as well as some islands. Compared to Fe-13Cr, increasing the Cr content transforms the corrosion islands into a continuous layer, increasing the scale thickness (see Figure 3c).

The line scans in Figure 4 show the elemental variation from the base alloy (left side) to the surface (right side).

Fe-13Cr shows constant Fe and Cr levels in the bulk alloy. Towards the surface, a small area (<1 μm) of Cr depletion below the alloy/scale interface is detected. The Cr depletion zone is the distance from the point where Cr levels fall below the nominal Cr amount to the surface of the alloy. The scale consists of Fe, Cr, and O. Sulfur was not detected by SEM-EDX.

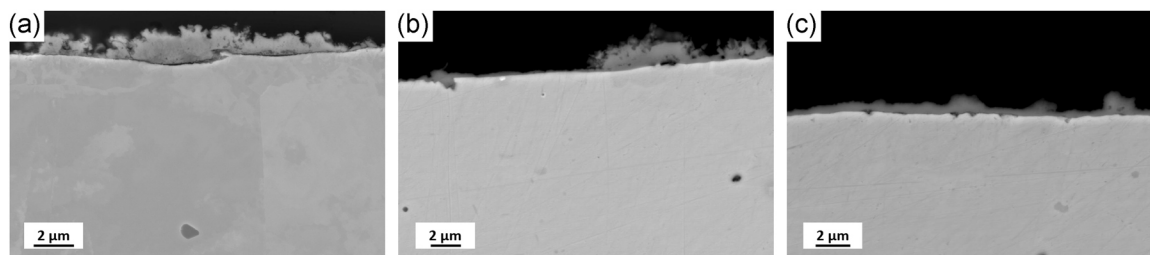


FIGURE 3 Scanning electron microscopy-backscattered electron images of samples exposed to 0.5%  $\text{SO}_2$ /99.5% Ar for 330 h at 560°C. (a) Fe-13Cr, (b) Fe-18Cr-12Ni, and (c) Fe-25Cr-20Ni

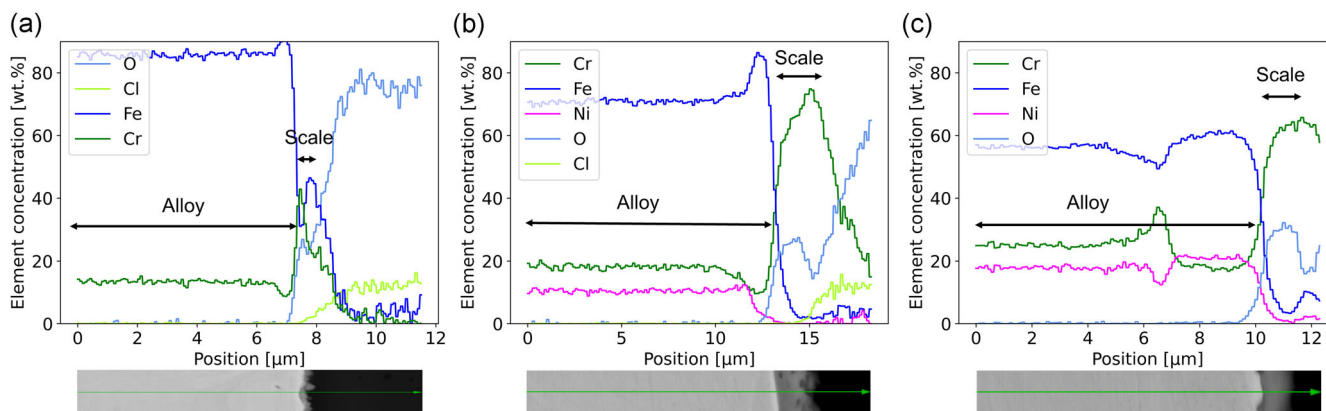


FIGURE 4 Line scans obtained by energy dispersive X-ray analysis of samples exposed to 0.5%  $\text{SO}_2$ /99.5% Ar for 330 h at 560°C. (a) Fe-13Cr, (b) Fe-18Cr-12Ni, and (c) Fe-25Cr-20Ni [Color figure can be viewed at [wileyonlinelibrary.com](http://wileyonlinelibrary.com)]

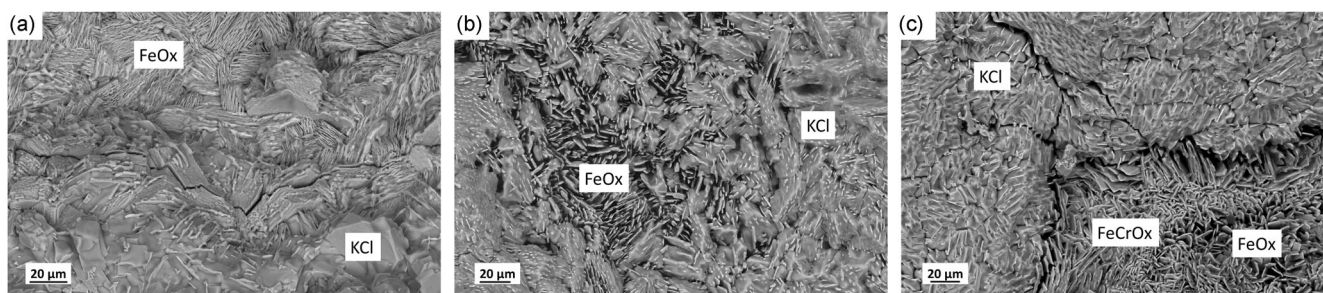


FIGURE 5 Backscattered electron surface images of samples (a) Fe-13Cr, (b) Fe-18Cr-12Ni, and (c) Fe-25Cr-20Ni exposed to 0.5%  $\text{SO}_2$ /99.5% Ar + KCl for 330 h at 560°C

Fe-18Cr-12Ni shows a homogeneous Fe, Cr, and Ni distribution in the base alloy. Just below the alloy/scale interface a larger Cr depletion zone ( $\sim 1\ \mu\text{m}$ ) is observed, while the scale consists of  $\text{Cr}_2\text{O}_3$ .

Fe-25Cr-20Ni shows constant amounts of Fe, Cr, and Ni. However,  $6\ \mu\text{m}$  below the surface a local enrichment of Cr at the cost of Fe and Ni is observed. This might be an artifact of insufficient homogenization during alloy preparation. Fe-25Cr-20Ni shows the deepest Cr depletion zone of all samples. The scale consists of  $\text{Cr}_2\text{O}_3$ .

## 3.2 | 0.5% $\text{SO}_2$ /99.5% Ar + KCl

### 3.2.1 | Surface structure and morphology—post-exposure

The SEM-BSE surface images of samples exposed to KCl deposits and 0.5%  $\text{SO}_2$  are depicted in Figure 5.

Fe-13Cr shows crystals of KCl and a densely packed, fiber-like iron oxide. Cracks can be observed along the surface.

Fe-18Cr-12Ni shows KCl crystals overgrown with individual needles of iron oxide. The iron oxide seems to grow in oriented plates. The thin side is oriented towards the surface with large vacancies in between iron oxide plates.

The surface of Fe-25Cr-20Ni after SO<sub>2</sub> exposure shows similar morphology to Fe-18Cr-12Ni. KCl crystals are observed with iron oxide needles overgrowing them. The KCl on top of the samples shows several cracks. The Fe-Cr-oxide (marked in Figure 5c) is denser than the iron oxide next to it. The iron oxide shows the same oriented plates as seen in Fe-18Cr-12Ni, the Fe-Cr-oxide grows randomly and does not show a clear orientation.

Figure 6 shows the surface EDX of Fe-13Cr after exposure to 0.5% SO<sub>2</sub>/99.5% Ar + KCl for 330 h at 560°C.

The surface shows two distinct structures: large crystals and a very porous phase below.

Figure 6a shows that the crystals are partially overgrown by a darker phase. Cross-referencing that with the elemental maps in Figure 6 shows that the darker phase consists of K, O, and S. The crystals underneath KCl.

The porous phase below and next to the crystals seem to consist of mainly iron oxides with some K and Cl being detected (see Figures 6b,c,d,f). The model alloys Fe-18Cr-12Ni and Fe-25Cr-20Ni show a similar surface composition, as verified by XRD (see Figure 7).

The scale of Fe-13Cr mainly consists of Fe<sub>2</sub>O<sub>3</sub> and KCl, as well as K<sub>2</sub>SO<sub>4</sub> (see Figure 7). Fe<sub>3</sub>O<sub>4</sub> and Cr<sub>2</sub>O<sub>3</sub>

were not identified in the scale of Fe-13Cr by XRD analysis.

Fe-18Cr-12Ni and Fe-25Cr-20Ni show a very similar diffraction pattern. Both show reflections corresponding to Fe<sub>2</sub>O<sub>3</sub>, Cr<sub>2</sub>O<sub>3</sub>, Fe<sub>3</sub>O<sub>4</sub>, KCl, and K<sub>2</sub>SO<sub>4</sub>.

### 3.2.2 | Cross-section analysis

The SEM-BSE cross-section images of KCl-exposed samples are shown in Figure 8 for comparison. All

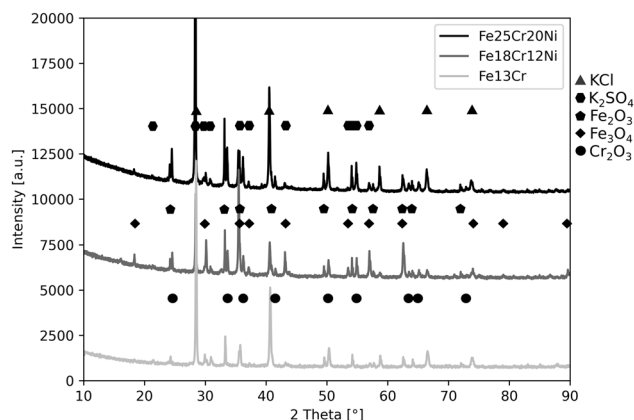


FIGURE 7 X-ray diffraction of 0.5% SO<sub>2</sub>/99.5% Ar + KCl-exposed samples

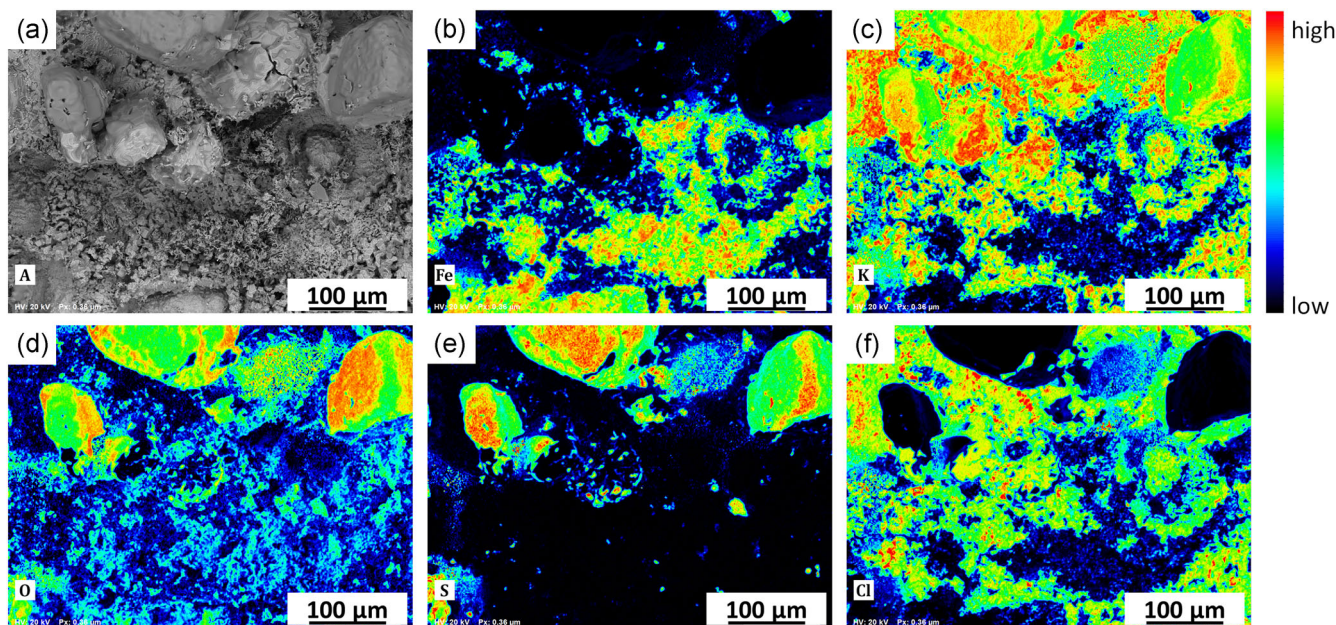


FIGURE 6 Surface scanning electron microscopy-energy dispersive X-ray analysis elemental distribution maps of Fe-13Cr exposed to 0.5% SO<sub>2</sub>/99.5% Ar + KCl for 330 h at 560°C, showing KCl overgrown by K<sub>2</sub>SO<sub>4</sub>. (a) shows the backscattered electron image of the surface and (b-f) the element maps [Color figure can be viewed at [wileyonlinelibrary.com](http://wileyonlinelibrary.com)]

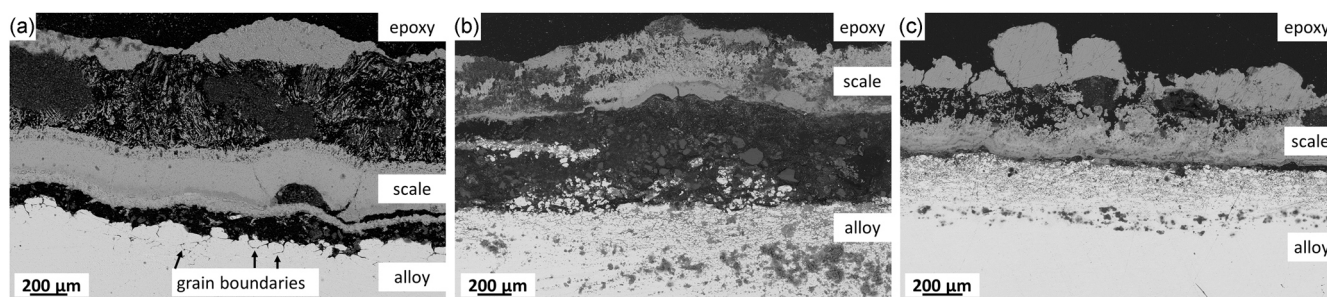


FIGURE 8 Scanning electron microscopy-backscattered electron images of samples (a) Fe-13Cr, (b) Fe-18Cr-12Ni, and (c) Fe-25Cr-20Ni exposed to 0.5% SO<sub>2</sub>/99.5% Ar + KCl for 330 h at 560°C

samples show a complex, multicomponent scale, that exceeds 100 μm.

Fe-13Cr (Figure 8a) shows a rough alloy/scale interface and only very little damage to the bulk alloy. The corrosion attack in the alloy seems to be limited to an area close to the alloy/scale interface along grain boundaries. The scale shows several distinct phases. The area closest to the alloy shows a rough morphology with small droplets. Further outward a thin and dark layer can be observed, separating the rough area from the large, light gray area, which ends in a porous, needle-like area.

Fe-18Cr-12Ni (Figure 8b) shows an extensive corrosion attack in the base alloy (henceforth called internal corrosion attack). Large patches of a rough, dark gray area can be seen within the alloy, as well as a large internal corrosion network. The scale consists of multiple components, which do not exhibit an orderly layering but instead are concentrated in different regions.

The scale of Fe-25Cr-20Ni (Figure 8c) is layered and shows subsurface damage similar to Fe-18Cr-12Ni. An internal corrosion attack caused a zone of rough, dark gray patches and an extensive corrosion network closer to the alloy/scale interface. The scale seems to consist of several layers though, more closely resembling Fe-13Cr's layered scale. It shows a dark layer close to the alloy/scale interface and a porous surface towards the scale/atmosphere interface.

Figure 9 shows the cross-section SEM-EDX of elemental distribution maps of Fe-13Cr after exposure to 0.5% SO<sub>2</sub>/99.5% Ar + KCl for 330 h at 560°C.

The sample shows Cr depletion along grain boundaries in the base alloy (see Figure 9d). At the alloy/scale interface S, Fe, and Cr are enriched (Figure 9f,b,d). Above the S layer, a high O concentration was observed (Figure 9e). At the former gas side interface, KCl is covering the scale (Figure 9c,g).

Figure 10 shows the cross-section SEM-EDX elemental distribution maps of Fe-18Cr-12Ni after exposure to 0.5% SO<sub>2</sub>/99.5% Ar + KCl for 330 h at 560°C.

The linescan in Figure 10i identifies the dark spots at around 300 μm to be FeCl<sub>2</sub>. The linescan furthermore shows a Fe and Cr depletion and a Ni enrichment towards the alloy/scale interface. The areas enriched in Ni show higher amounts of O.

The scale shows Cr enrichment at the alloy/scale interface along with O or Cl. Notably, this sample shows a thick and porous Cr<sub>2</sub>O<sub>3</sub>/CrCl<sub>3</sub> layer ( $d \sim 80 \mu\text{m}$ ) close to the alloy/scale interface (seen in Figure 10d,e,g). Fe is predominantly found at the scale/atmosphere interface in conjunction with O.

Figure 11 shows the cross-section SEM-EDX elemental distribution maps of Fe-25Cr-20Ni after exposure to 0.5% SO<sub>2</sub>/99.5% Ar + KCl for 330 h at 560°C.

Similar to Fe-18Cr-12Ni, Fe-25Cr-20Ni (Figure 11i) shows areas of chloride formation deep within the bulk alloy. This is followed by a Ni enrichment towards the alloy/scale interface at the cost of Fe and Cr, reaching Ni contents of up to 50 wt% at the interface (see Figure 11i).

The scale at the alloy/scale interface consists of Cr, S, and O (see Figure 11d,f,e). Towards the former gas side Fe concentration increases at the expense of Cr (Figure 11b,d). S is only found close to the alloy/scale interface, as CrS closer to the metal and as FeS in the outer layer. The scale/gas interface consists of Fe and O.

## 4 | DISCUSSION

### 4.1 | Main results

The experiments show the growth of a thin scale in a 0.5% SO<sub>2</sub>/99.5% Ar atmosphere for all samples (Figure 12). The scale consists of Cr<sub>2</sub>O<sub>3</sub> and Fe<sub>2</sub>O<sub>3</sub> in the case of Fe-13Cr. Both higher alloyed samples formed Cr<sub>2</sub>O<sub>3</sub> instead and showed spallation of the scale.

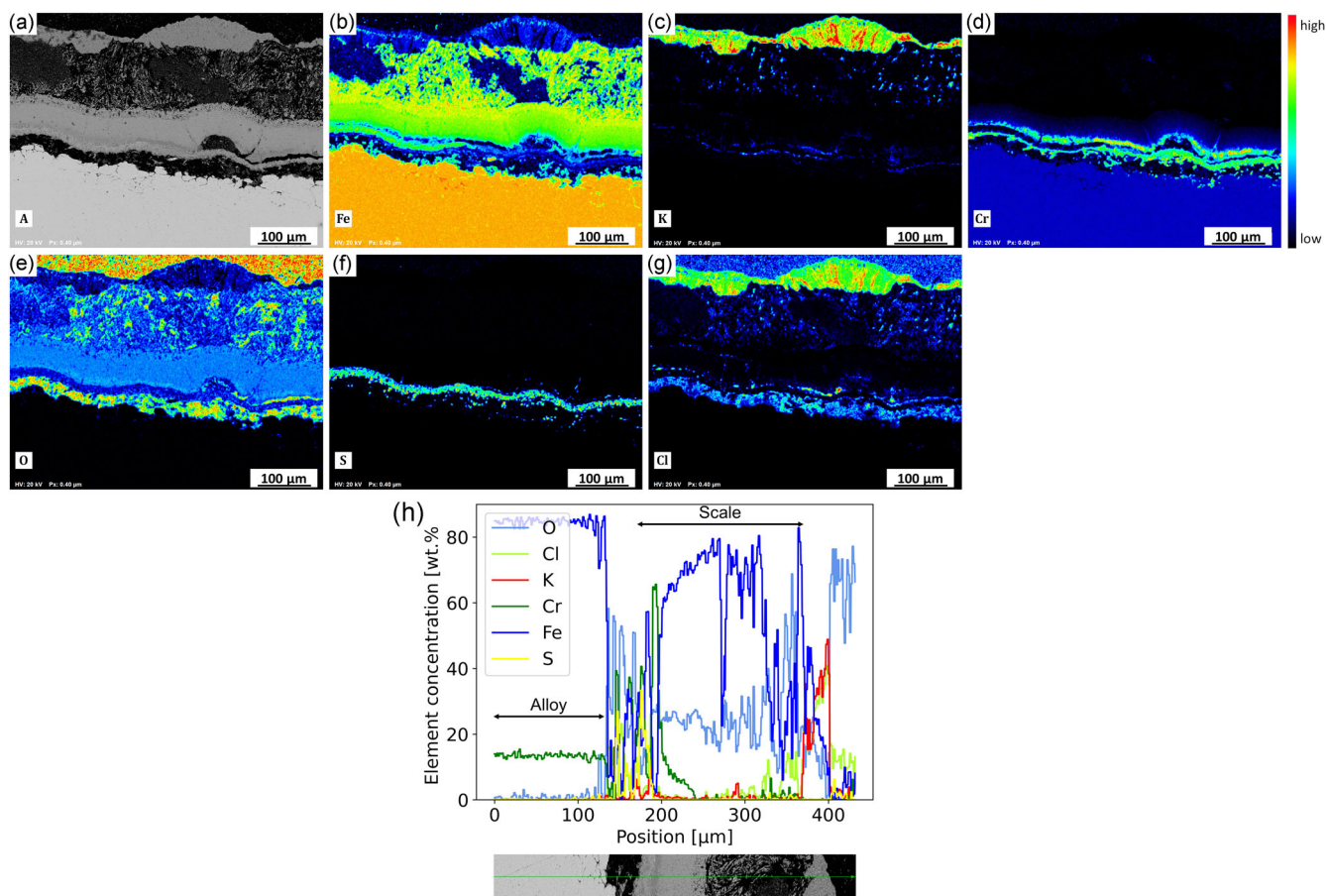


**FIGURE 9** Cross section scanning electron microscopy-energy dispersive X-ray analysis elemental distribution maps of Fe-13Cr exposed to 0.5% SO<sub>2</sub>/99.5% Ar + KCl for 330 h at 560°C. (a) shows the backscattered electron image and (b–g) element maps. (h) shows the linescan from the base alloy to the gas [Color figure can be viewed at [wileyonlinelibrary.com](http://wileyonlinelibrary.com)]

- Thin oxide scale on all samples
- Spallation of the scale

Samples exposed to 0.5% SO<sub>2</sub>/99.5% Ar + KCl show a large corrosion attack with scales exceeding 100 μm (see Figure 12). The addition of KCl leads to the formation of K<sub>2</sub>SO<sub>4</sub> as well as an extensive scale of iron oxides, Cr<sub>2</sub>O<sub>3</sub>, FeS, and CrS.

The alloys Fe-18Cr-12Ni and Fe-25Cr-20Ni show internal corrosion, forming Fe- and Cr chlorides and enriching the alloy/scale interface in Ni.

- Large multicomponent scale consisting of FeS, CrS, Fe<sub>3</sub>O<sub>4</sub>, Fe<sub>2</sub>O<sub>3</sub>, and Cr<sub>2</sub>O<sub>3</sub>
- Densely packed Fe<sub>2</sub>O<sub>3</sub> at a surface of Fe-13Cr (ferritic), ferritic-austenitic samples showed a lower density
- Ferritic-austenitic samples showed strong internal corrosion
- Ferritic-austenitic samples showed Ni enrichment at the alloy/scale interface

## 4.2 | 0.5% SO<sub>2</sub>/99.5% Ar atmosphere

### 4.2.1 | Influence of Cr and microstructure

The SEM-EDX linescan on the cross-section of Fe-13Cr after gas exposure (Figure 4a) shows that Fe-13Cr formed a scale consisting of Fe and Cr oxides. Increasing the Cr content to 18 wt% (Fe-18Cr-12Ni) or higher caused Cr<sub>2</sub>O<sub>3</sub> formation (see Figure 4b,c). The increasing amount of Cr in the corrosion product is clearly linked to the increasing Cr content in the bulk material. All samples show a Cr depletion zone just under the scale, which increases with increasing Cr content. This is likely due to Cr<sub>2</sub>O<sub>3</sub> formation needing more Cr to form compared to a mixed Fe and Cr oxide scale. The microstructure is also noteworthy being different for the three alloys. Fe-13Cr is purely ferritic as opposed to the ferritic-austenitic microstructure of Fe-18Cr-12Ni and Fe-25Cr-20Ni (see Table 1). Calculating the diffusion coefficient at 560°C, in a matrix made purely of Fe, using the formulas (see

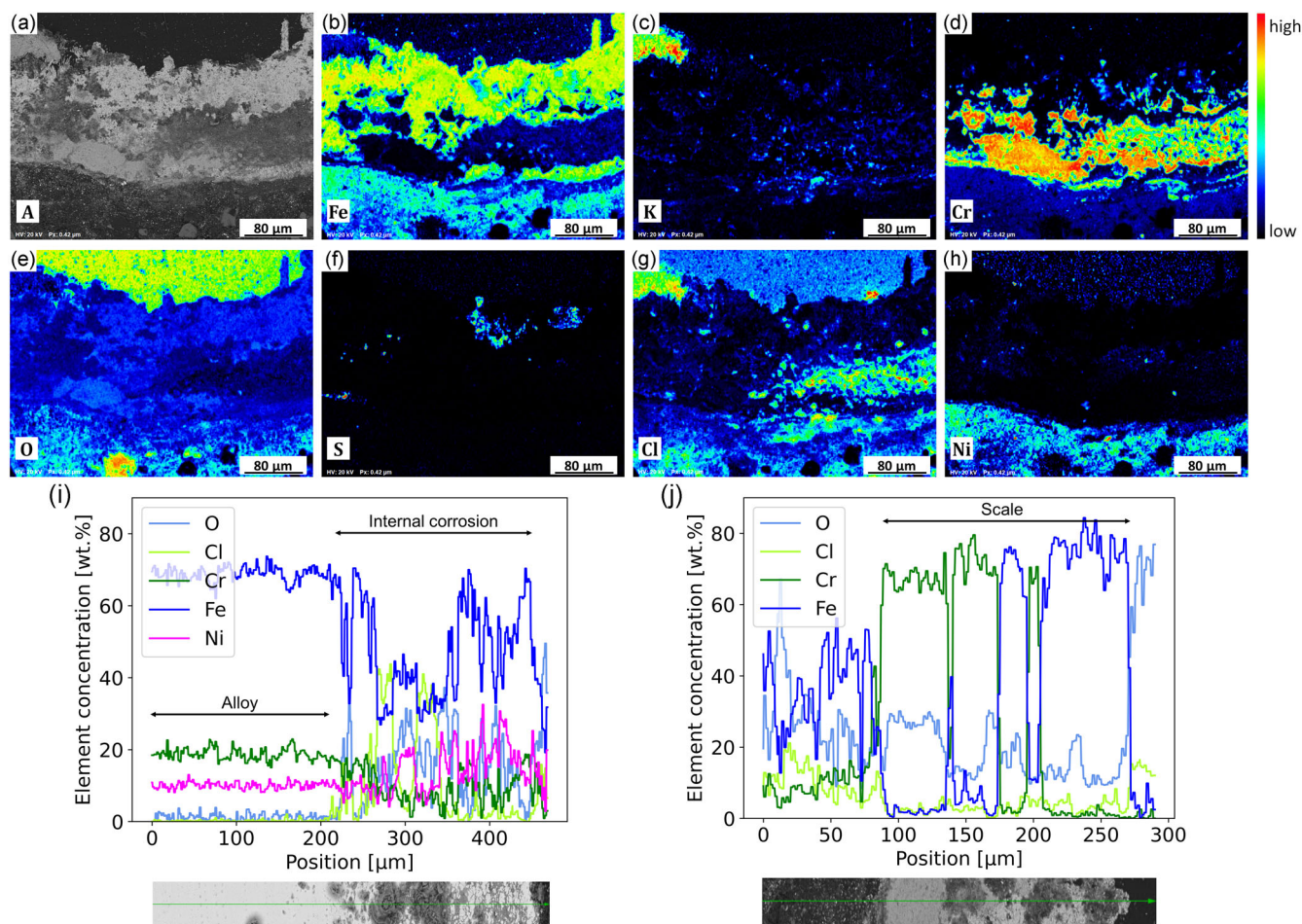


**FIGURE 10** Cross section scanning electron microscopy–energy dispersive X-ray analysis elemental distribution maps of Fe–18Cr–12Ni exposed to 0.5% SO<sub>2</sub>/99.5% Ar + KCl for 330 h at 560°C. (a) shows the backscattered electron image and (b–h) element maps. (i) shows the linescan through the metal and (j) the linescan through the scale [Color figure can be viewed at [wileyonlinelibrary.com](http://wileyonlinelibrary.com)]

Table 3) given by Buffington et al.,<sup>[10]</sup> Bowen et al.<sup>[11]</sup> and Hirano et al.<sup>[12]</sup> leads to the values displayed in Table 4. The diffusion coefficients show, that every metal present in the model alloys diffuses much quicker in a ferritic matrix as compared to an austenitic one. This explains the thinner Cr depletion zone in the ferritic Fe–13Cr and the larger Cr depletion in the ferritic–austenitic Ni-bearing steels.

### 4.3 | 0.5% SO<sub>2</sub>/99.5% Ar + KCl

#### 4.3.1 | Sample surface

The salt bearing surface shown in Figure 6 is representative of all studied samples. K<sub>2</sub>SO<sub>4</sub> overgrows the KCl crystals when exposed to SO<sub>2</sub>. K<sub>2</sub>SO<sub>4</sub> was also confirmed in all samples by the XRD experiments, as shown in Figure 7. The shape of the grain boundaries and the smooth texture of K<sub>2</sub>SO<sub>4</sub> indicate that it melted during

the exposure. This is surprising, considering neither KCl nor K<sub>2</sub>SO<sub>4</sub> melt at 560°C.<sup>[13]</sup> Okoro et al.<sup>[13]</sup> observed the same phenomenon and explained it through the formation of a eutectic mixture of KCl and Fe or Cr chlorides, where melting temperatures were observed between 200°C and 500°C.<sup>[14]</sup>

#### 4.3.2 | Impact of Ni and Cr

Overall Ni-bearing samples seem to be more susceptible to corrosion attack. Comparing the internal corrosion of Fe–13Cr and Fe–18Cr–12Ni in Figure 8a,b, the internal corrosion affects a much larger zone and leads to different corrosion products if Ni is present. A similar result can be observed for Fe–25Cr–20Ni in Figure 8c.

Figure 13a shows the location of detected chlorides within the base alloy. The penetration depth denotes the distance from the alloy/scale interface to the position of the chlorides.



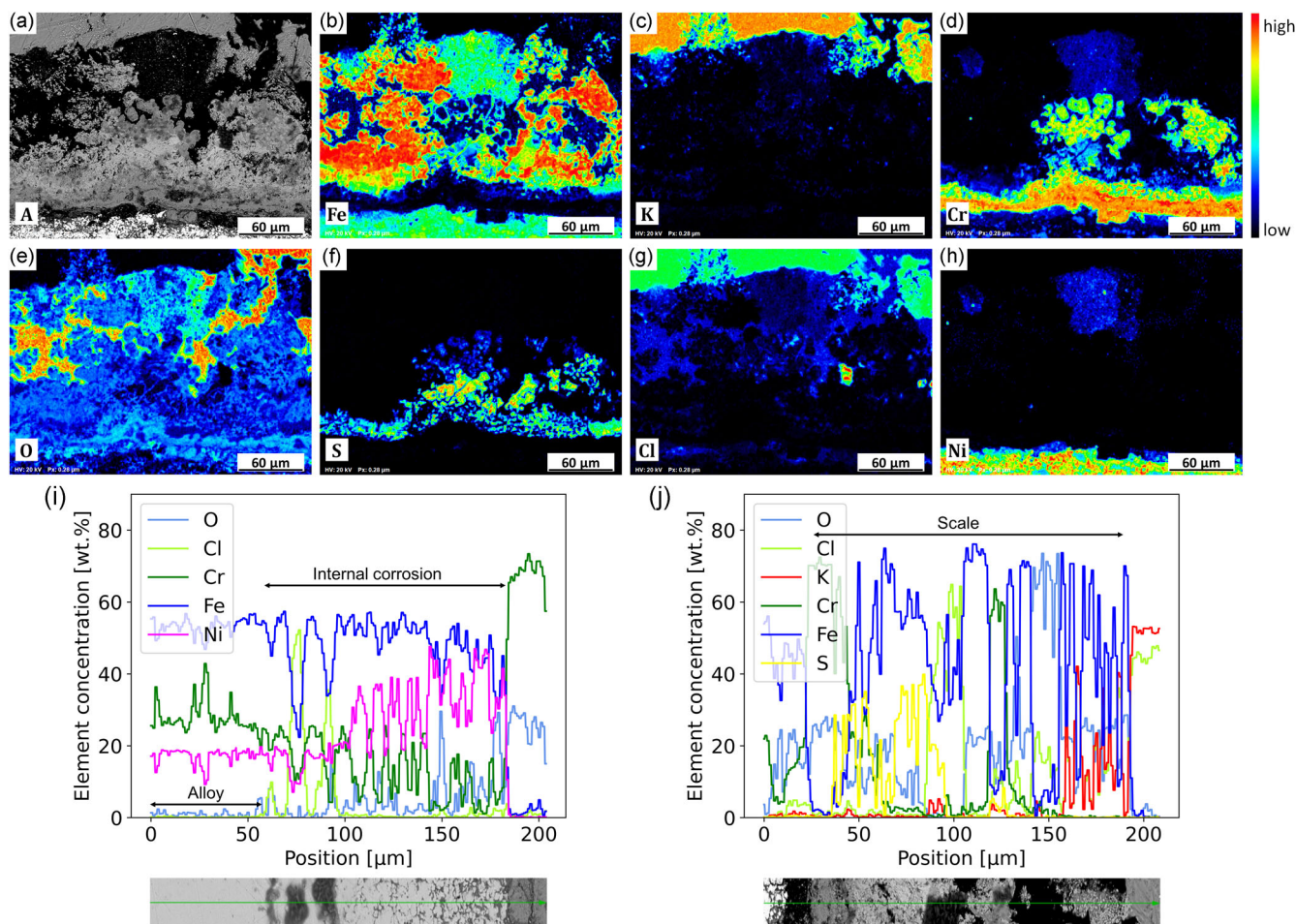


**FIGURE 11** Cross section scanning electron microscopy-energy dispersive X-ray analysis elemental distribution maps of Fe-25Cr-20Ni exposed to 0.5% SO<sub>2</sub>/99.5% Ar + KCl for 330 h at 560°C. (a) shows the backscattered electron image and (b-h) element maps. (i) shows the linescan through the metal and (j) the linescan through the scale [Color figure can be viewed at [wileyonlinelibrary.com](http://wileyonlinelibrary.com)]

Fe-13Cr did not form any chlorides within the base alloy. However, alloying with Ni caused chlorides to form within a zone in the alloy. For Fe-18Cr-12Ni, the chloride zone started at  $225 \pm 69 \mu\text{m}$  and extended until  $578 \pm 134 \mu\text{m}$ . Fe-25Cr-20Ni showed a much narrower zone from  $235 \pm 22 \mu\text{m}$  to  $313 \pm 29 \mu\text{m}$ .

Figure 13b shows the average internal corrosion zone and the scale thickness. The internal corrosion zone grows noticeably in the Ni alloyed system. Fe-13Cr shows comparatively low internal corrosion at  $61 \pm 35 \mu\text{m}$ . The introduction of Ni into the alloy leads to an internal corrosion zone of  $1013 \pm 85 \mu\text{m}$  for sample Fe-18Cr-12Ni. Further increasing the amount of Ni and Cr reduces the internal corrosion area significantly to  $314 \pm 19 \mu\text{m}$  in sample Fe-25Cr-20Ni. By comparison, the scale thickness only slightly varies between Fe-13Cr and Fe-18Cr-12Ni, however, Fe-25Cr-20Ni shows a thinner scale.

The results from Figure 13 in combination with the Ni enrichment observed in Figures 10 and 11i point

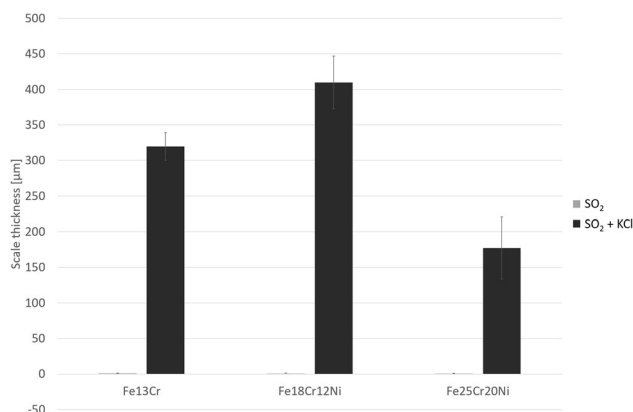


**FIGURE 12** Comparison of the scale thickness developed in a pure 0.5% SO<sub>2</sub> containing atmosphere compared to SO<sub>2</sub> + KCl

towards Ni being a detriment to the corrosion resistance of deposit-induced corrosion. The presence of Ni leads to the formation of both chlorides as well as nickel oxides in the base alloy.

TABLE 3 Diffusion coefficient formulas for  $D$  (cm<sup>2</sup>/s),  $R$  = gas constant (J/Kmol)<sup>[10–12]</sup>

Diffusing element	Fe	Cr	Ni
In $\alpha$ – Fe	$2.0 \times e^{\frac{-60000}{R \times 833.15K}}$	$8.52 \times e^{\frac{-59900}{R \times 833.15K}}$	$1.4 \times e^{\frac{-58700}{R \times 833.15K}}$
In $\gamma$ – Fe	$0.18 \times e^{\frac{-64500}{R \times 833.15K}}$	$10.8 \times e^{\frac{-69700}{R \times 833.15K}}$	$0.77 \times e^{\frac{-67000}{R \times 833.15K}}$

TABLE 4 Calculated diffusion coefficient  $D$  (cm<sup>2</sup>/s) at 560°C

Diffusing element	Fe	Cr	Ni
In $\alpha$ – Fe	$3.5 \times 10^{-4}$	$1.5 \times 10^{-3}$	$2.9 \times 10^{-4}$
In $\gamma$ – Fe	$1.6 \times 10^{-5}$	$4.6 \times 10^{-4}$	$4.9 \times 10^{-5}$

The negative effect of SO<sub>2</sub> on the corrosion behavior of Ni-based superalloys has been shown by both Huczowski et al.<sup>[15]</sup> and Oleksak et al.<sup>[16]</sup> at temperature ranges 550–650°C. Oleksak et al. saw mass changes in all studied samples at 600°C with a mass change factor of 2390 comparing 95% CO<sub>2</sub>/4% H<sub>2</sub>O/1% O<sub>2</sub> atmosphere to the same atmosphere with 0.1% SO<sub>2</sub> in alloy 617. Huczowski et al. and Oleksak et al. determined that the poor corrosion behavior is due to the transition from oxides to sulfates. Due to the enrichment of Ni at the alloy/scale interface for samples Fe–18Cr–12Ni and Fe–25Cr–20Ni (Figures 10 and 11i) it is reasonable to assume a similar behavior in these samples, however, sulfates replacing oxides was not observed.

On the basis of the distribution of Cr in Figures 9–11, the likely cause for the different internal oxidation behavior is the density of the Cr layer. Fe–13Cr shows a thin but dense layer of Cr<sub>2</sub>O<sub>3</sub> which provides a diffusion barrier for Cl. Comparing this to the Cr distribution in Fe–18Cr–12Ni (Figure 10d) it is evident that the Cr<sub>2</sub>O<sub>3</sub> is not dense enough to protect the metal from further Cl corrosion. Fe–25Cr–20Ni shows a denser layer of Cr<sub>2</sub>O<sub>3</sub>. The dense Cr<sub>2</sub>O<sub>3</sub> layer is a diffusion barrier for Cl, which is reflected in the smaller internal corrosion area is shown in Figure 13b. The beneficial effect of the increased amount of Cr outweighs the potential downside of increased Ni in the form of Ni-sulfides or an increasing amount of austenite.

#### 4.3.3 | Impact of the microstructure

Finally, the microstructure needs to be considered concerning its impact on the corrosion behavior, as the addition of Ni changes the microstructure from purely ferritic to ferritic–austenitic.<sup>[17]</sup> When comparing the purely ferritic Fe–13Cr with the ferritic–austenitic

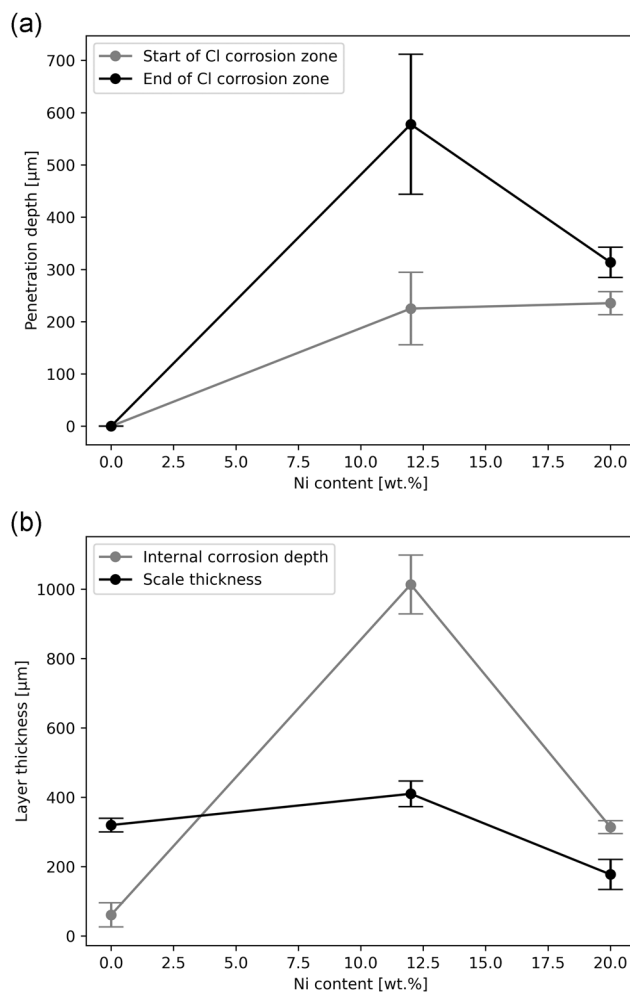


FIGURE 13 Effect of alloying elements on corrosion behavior. (a) Cl penetration depth and (b) zone affected by corrosion. Sample Fe–13Cr (at 0 wt% Ni in the graphs) is purely ferritic, the samples Fe–18Cr–12Ni and Fe–25Cr–20Ni are ferritic–austenitic

Fe–18Cr–12Ni and Fe–25Cr–20Ni the difference in internal corrosion area is evident (see Figure 13a).

The impact of the microstructure of a Fe–16Cr–0.2C alloy on the corrosion behavior in an SO<sub>2</sub> bearing atmosphere has recently been studied by Falk et al.<sup>[18]</sup> The study showed that the microstructure impacts the formed product. A much thinner corrosion layer was formed on ferritic grains compared to bainitic ones which was attributed to much faster diffusion paths in bainite.

The slower diffusion of Fe and Cr in austenite, as shown in Table 4, is likely a reason for the comparatively poor performance of the ferritic–austenitic alloys compared to the ferritic Fe–13Cr. The diffusion coefficient at 560°C is an order of magnitude larger in ferrite compared to austenite. The effect of the lower diffusion velocity, at a constant exposure time of 330 h, can be observed in the linescans. Fe–13Cr (Figure 9h) shows no Cr depletion. Both Fe–18Cr–12Ni (Figure 10i) and Fe–25Cr–20Ni

(Figure 11i) show a severe Cr depletion towards the alloy/scale interface. This is likely due to the slower diffusion of Fe and Cr in the austenite, which is detrimental in the event of spallation.

The microstructure also has an impact on the grain orientation and density of the formed corrosion product. The samples exposed to 0.5% SO<sub>2</sub>/99.5% Ar + KCl show highly oriented grains at the surface, in particular for the partially austenitic samples Fe–18Cr–12Ni and Fe–25Cr–20Ni (see Figure 5b,c).

The orientation relation of ferrite, magnetite, and hematite has been shown previously by Stephan-Scherb et al.<sup>[19]</sup> The orientation of hematite is therefore likely due to the orientation of the phase below it. The large gaps between hematite plates could therefore be due to an energetically unfavorable orientation of the phase below, leading to selective hematite growth and a lower density. The impact can be seen in the internal corrosion (Figure 8), which shows a much stronger attack in the austenitic-ferritic samples (Fe–18Cr–12Ni and Fe–25Cr–20Ni) when compared to the ferritic Fe–13Cr. The density of the iron oxides in sample Fe–13Cr (see Figure 5a) is much higher than in samples Fe–18Cr–12Ni and Fe–25Cr–20Ni (Figures 5b,c). The higher density hinders the transport of Cl<sub>2</sub> through the scale, limiting the corrosion attack.

The increase of Ni at the alloy/scale interface is likely due to the formation of FeCl<sub>2</sub> and CrCl<sub>2</sub>. NiCl<sub>2</sub> is not formed, since the Gibbs energy is highest for NiCl<sub>2</sub> (–174.2 kJ/mol at 600°C) in comparison to FeCl<sub>2</sub> and CrCl<sub>2</sub> (–232.1 and –286.0 kJ/mol at 600°C respectively).<sup>[20,21]</sup> This causes Ni to enrich at the interface which then partially reacts with available oxygen to form NiO. The Cl attack seems to depend on the microstructure of the alloy. The ferritic sample shows very little internal corrosion, while the ferritic-austenitic samples showed a much more extensive internal corrosion zone. Increasing the amount of Cr is beneficial for corrosion resistance, leading to a smaller internal corrosion zone. This is in line with the results shown by Montero et al.,<sup>[22]</sup> who observed a Ni enrichment and showed that Ni-based alloys demonstrated a lower corrosion resistance in lignite combustion than austenitic steels and the beneficial effect of Cr. Montero et al. attributed the detrimental effect of Ni to breakaway caused by NiS as well as NiSO<sub>4</sub>, which can promote hot corrosion. This is counteracted by Cr through the protective properties of Cr<sub>2</sub>O<sub>3</sub>.

#### 4.3.4 | Attack mechanism

Unlike the KCl corrosion in oxidizing atmospheres, the onset of Cl-induced corrosion in SO<sub>2</sub> is likely different. In

oxidizing environments, the formation of K<sub>2</sub>CrO<sub>4</sub> was observed.<sup>[4,5,7]</sup>

Experiments were conducted with comparable steel (304L, Fe–18Cr–10Ni) at 600°C by Pettersson<sup>[5]</sup> in an oxidizing atmosphere (5% O<sub>2</sub>/95% N<sub>2</sub> + KCl) and Karlsson et al.<sup>[7]</sup> in a humid atmosphere (5% O<sub>2</sub>/40% H<sub>2</sub>O/300 ppm SO<sub>2</sub>/N<sub>2</sub> + KCl) showed that the initial reaction involved the destruction of Cr<sub>2</sub>O<sub>3</sub> to form K<sub>2</sub>CrO<sub>4</sub>. In the present study, no K<sub>2</sub>CrO<sub>4</sub> could be detected, presumably due to the lower amount of oxygen (0.5% SO<sub>2</sub> [pO<sub>2</sub> = 1 × 10<sup>–16</sup>] vs. Pettersson's 5% O<sub>2</sub>[SO<sub>2</sub> = 5 × 10<sup>–2</sup>]) available. Instead, K<sub>2</sub>SO<sub>4</sub> was verified through EDX and XRD. In Karlsson's humid atmosphere<sup>[7]</sup> K<sub>2</sub>SO<sub>4</sub> was also identified as the reaction product of K<sub>2</sub>CrO<sub>4</sub> and SO<sub>2</sub>.

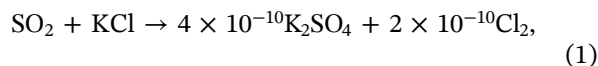
Besides K<sub>2</sub>SO<sub>4</sub> no other sulfates were found in our experiments, likely due to the low oxygen partial pressure. A Factsage 8.0 calculation shows that at the given sulfur partial pressure, an oxygen partial pressure of 10<sup>–13</sup> or higher would be required to form stable metal sulfates. Therefore, only metal sulfides are expected.

This means, that in the presence of SO<sub>2</sub> the KCl prefers to form K<sub>2</sub>SO<sub>4</sub> instead of attacking Cr<sub>2</sub>O<sub>3</sub>. This supports the beneficial properties found for sulfur-containing compounds in biofuel combustion. This could imply a better corrosion behavior of steels in atmospheres containing SO<sub>2</sub>.

Several authors<sup>[23–25]</sup> have found a beneficial effect through the addition of sulfates and sulfur. Aho et al.<sup>[23]</sup> showed that introducing Fe<sub>2</sub>SO<sub>4</sub> reduces the mass flow of Cl through the formation of SO<sub>2</sub>, which can prevent Cl deposition or reduce high-temperature chlorine-induced corrosion. Davidsson et al.<sup>[24]</sup> showed, that elemental S and (NH<sub>4</sub>)<sub>2</sub>SO<sub>4</sub> reduced KCl in the flue gas, leading to a reduction of KCl deposits.

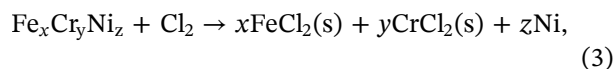
On the basis of the findings in this study and thermodynamic calculations (using FactSage 8.0), the reaction of KCl and SO<sub>2</sub> with chromium-rich steels happens in multiple stages. Only the relevant phases are shown in the reactions below.

First, the atmospheric SO<sub>2</sub> reacts with the KCl deposits on the sample surface. This leads to the formation of K<sub>2</sub>SO<sub>4</sub>, which was shown through EDX and XRD analysis in Figures 6 and 7.



$$dG = -1.2 \times 10^{-2} \text{J}. \quad (2)$$

This initial reaction provides Cl<sub>2</sub>, which can then attack the metal.



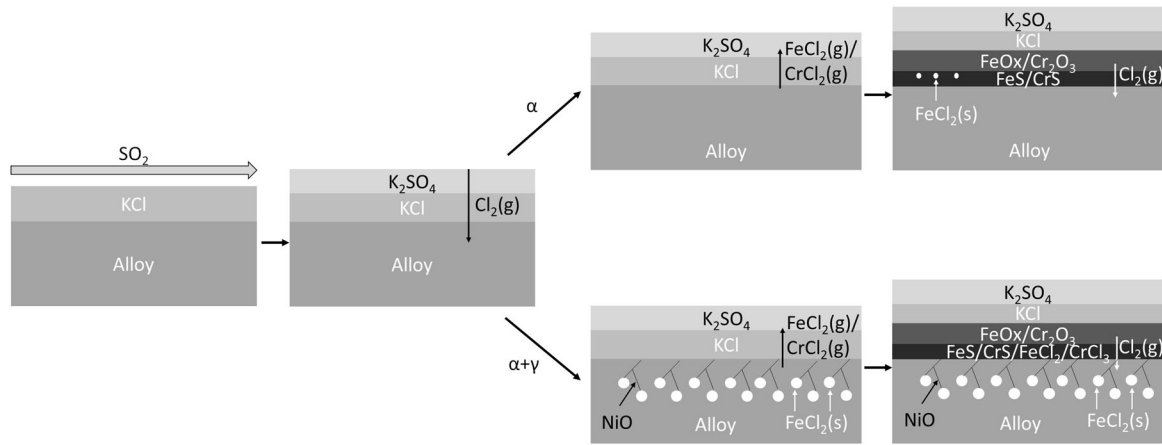
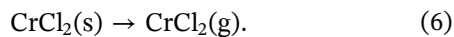
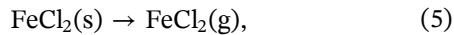


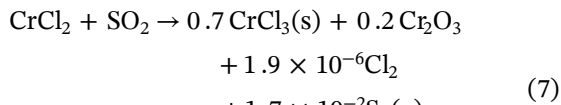
**FIGURE 14** Schematic overview of the proposed corrosion mechanism depending on the microstructure.  $\alpha$  denotes ferritic steels (i.e., Fe-13Cr),  $\alpha + \gamma$  the ferrite+austenite samples (i.e., Fe-18Cr-12Ni and Fe-25Cr-20Ni)

$$dG \approx -2.5 \times 10^5 \text{ J.} \quad (4)$$

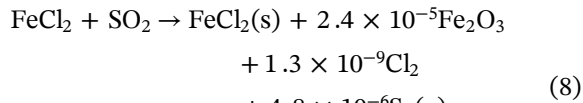
$\text{CrCl}_2$  and  $\text{FeCl}_2$  have a high evaporation pressure.<sup>[21]</sup> For  $\text{FeCl}_2$  considerable evaporation is expected above  $536^\circ\text{C}$ .<sup>[26]</sup>



$\text{CrCl}_2(\text{g})$  and  $\text{FeCl}_2(\text{g})$  are then transported towards the surface, where the sulfur and oxygen partial pressures are high enough to initiate the reaction:



$$dG = -1.3 \times 10^5 \text{ J.}$$



$$dG = -4.7 \times 10^4 \text{ J.}$$

The sulfur can then react with the alloy to form FeS, CrS and NiS.

This reaction is responsible for the scale growth and provides the Cl needed to continue the active Cl corrosion, as described by Grabke,<sup>[27]</sup> with  $\text{Cl}_2$  attacking the base alloy and forming Fe and Cr chlorides. These transform into a gas to once again react towards the surface with  $\text{SO}_2$  to form new Fe and Cr oxides and set free  $\text{Cl}_2$ .

A schematic overview of the corrosion mechanism is depicted in Figure 14.

## 5 | CONCLUSION

This study shows the impact of KCl in a 0.5%  $\text{SO}_2/99.5\%$  Ar environment on ferritic and ferritic-austenitic steel alloys, highlighting the importance of the alloying elements Cr and Ni on corrosion behavior.

All model alloys showed very little corrosion in a pure  $\text{SO}_2$  environment. They developed a thin, protective scale consisting of  $\text{Cr}_2\text{O}_3$ . Fe-13Cr additionally formed  $\text{Fe}_2\text{O}_3$ . All samples showed a small region of Cr depletion underneath the scale, which increased with increasing amounts of Cr in the alloy. This is likely due to the spallation that was observed with higher amounts of Cr as well as the Ni-induced microstructure change<sup>[17]</sup> from purely ferritic to ferritic-austenitic, causing a slower diffusion rate.

KCl induced corrosion caused extensive damage to the alloy. The samples all showed a thick scale consisting of Fe and Cr oxides and sulfides. Ni-containing samples showed a large internal corrosion zone beneath the original sample surface. This was especially pronounced in the Fe-18Cr-12Ni sample, showing an internal corrosion layer thickness of up to 1 mm. The Ni-containing samples showed a Ni enrichment towards the alloy/scale interface, which is attributed to extensive Cl attacks and the formation of NiO. Ni enrichment can lead to a poorer corrosion resistance through the formation of Ni-sulfides and -sulfates.<sup>[15,16,22]</sup>

## ACKNOWLEDGMENTS

The authors would like to thank Johannes Vrijmoed for valuable thermodynamic discussions and assistance with the SEM and Moritz Liesegang for assistance with the electron microprobe analysis and XRD measurements.

This study was funded by the German Research Foundation (DFG-416318834). Open Access funding enabled and organized by Projekt DEAL.

### CONFLICT OF INTERESTS

The authors declare that there are no conflicts of interest.


### AUTHOR CONTRIBUTIONS

**Phillip Kingsbery:** analysis, investigation, writing—original draft and visualization. **Christiane Stephan-Scherb:** conceptualization, supervision, writing—review and editing

### DATA AVAILABILITY STATEMENT

The raw data required to reproduce these findings cannot be shared at this time as the data also forms part of an ongoing study.

### ORCID

Phillip Kingsbery  <http://orcid.org/0000-0002-0401-2450>  
Christiane Stephan-Scherb  <http://orcid.org/0000-0001-6775-0023>

### REFERENCES

- [1] Y. Shao, J. Wang, F. Preto, J. Zhu, C. C. Xu, *Energies* **2012**, *5*, 5171.
- [2] H. P. Nielsen, F. J. Frandsen, K. Dam-Johansen, L. L. Baxter, *Prog. Energy Combust. Sci.* **2000**, *26*, 283.
- [3] A. Hernas, M. Imosa, B. Formanek, J. Cizner, *J. Mater. Process. Technol.* **2004**, *157–158*, 348.
- [4] J. Lehmusto, M. Sattari, M. Halvarsson, L. Hupa, *Corros. Sci.* **2021**, *183*, 109332.
- [5] J. Pettersson, H. Asteman, J.-E. Svensson, L.-G. Johansson, *Oxid. Metals* **2005**, *64*, 23.
- [6] T. Jonsson, J. Froitzheim, J. Pettersson, J.-E. Svensson, L.-G. Johansson, M. Halvarsson, *Oxid. Metals* **2009**, *72*, 213.
- [7] S. Karlsson, T. Jonsson, J. Hall, J.-E. Svensson, J. Liske, *Energy Fuels* **2014**, *28*, 3102.
- [8] K. B. Yoo, Y. He, H. S. Lee, S. Y. Bae, D. S. Kim, *KEPCO J. Electr. Power Energy* **2018**, *4*, 25.
- [9] *ISO 17224:2015(E)*. Corrosion of metals and alloys—Test method for high-temperature corrosion testing of metallive materials by application of a deposit of salt, ash, or other substances, International Organization for Standardization, Geneva, CH, **2015**.
- [10] F. S. Buffington, K. Hirano, M. Cohen, *Acta Metall.* **1961**, 434.
- [11] A. W. Bowen, G. M. Leak, *Metall. Trans.* **1970**, 1695.
- [12] K. Hirano, M. Cohen, B. L. Averbach, *Acta Metall.* **1961**, 440.
- [13] S. C. Okoro, M. Montgomery, F. J. Frandsen, K. Pantleon, *Energy Fuels* **2014**, *28*, 6447.
- [14] H. P. Michelsen, F. Frandsen, K. Dam-Johansen, O. H. Larsen, *Fuel Process. Technol.* **1998**, *54*, 95.
- [15] P. Huczkowski, D. J. Young, T. Olszewski, A. Chyrkin, W. J. Quadackers, *Oxid. Metals* **2018**, *89*, 651.
- [16] R. P. Oleksak, J. H. Tylczak, G. R. Holcomb, Ö. N. Doğan, *JOM* **2020**, *72*, 1822.
- [17] W. Bleck (Ed.), *Werkstoffkunde Stahl für Studium und Praxis*, 5th ed., Verlag Mainz, Aachen, Germany **2014**.
- [18] F. Falk, O. Sobol, C. Stephan-Scherb, *Corros. Sci.* **2021**, 190.
- [19] C. Stephan-Scherb, M. Menneken, K. Weber, L. AgudoJácome, G. Nolze, *Corros. Sci.* **2020**, *174*, 108809.
- [20] H. J. Grabke, M. Spiegel, A. Zahs, *Mater. Res.* **2004**, *7*, 89.
- [21] A. Zahs, M. Spiegel, H. J. Grabke, *Corros. Sci.* **2000**, *42*, 1093.
- [22] X. Montero, M. Rudolphi, M. C. Galetz, *Mater. Corros.* **2019**, *70*, 2179.
- [23] M. Aho, K. Paakinen, R. Taipale, *Fuel* **2013**, *103*, 562.
- [24] K. O. Davidsson, L.-E. Åmand, B.-M. Steenari, A.-L. Elled, D. Eskilsson, B. Leckner, *Chem. Eng. Sci.* **2008**, *63*, 5314.
- [25] Y. Zheng, P. A. Jensen, A. D. Jensen, B. Sander, H. Junker, *Fuel* **2007**, *86*, 1008.
- [26] H. J. Grabke, *Mater. High Temp.* **1993**, *11*, 23.
- [27] H. J. Grabke, E. Reese, M. Spiegel, *Corros. Sci.* **1995**, *37*, 1023.

**How to cite this article:** P. Kingsbery, C. Stephan-Scherb, *Mater. Corros.* **2022**, 1–13.  
<https://doi.org/10.1002/maco.202112901>